Waves in intensity coherence of evolving intense twin beams

Radek Machulka*

Joint Laboratory of Optics, Institute of Physics of the Czech Academy of Sciences, 17. listopadu 50a, 771 46 Olomouc, Czech Republic

Jan Peřina Jr.[†]

Joint Laboratory of Optics, Faculty of Science, Palacký University, 17. listopadu 12, 771 46 Olomouc, Czech Republic

Ondřej Haderka

Joint Laboratory of Optics, Faculty of Science, Palacký University, Czech Republic, 17. listopadu 12, 771 46 Olomouc, Czech Republic

Alessia Allevi

Dipartimento di Scienza e Alta Tecnologia, Università degli Studi dell'Insubria, Via Valleggio 11, 22100 Como, Italy

Maria Bondani

Istituto di Fotonica e Nanotecnologie, Consiglio Nazionale delle Ricerche, Via Valleggio 11, 22100 Como, Italy

Strong correlations between the signal and idler beams imprinted during their generation dominantly determine the properties of twin beams. They are also responsible for the waves in intensity coherence observed in the wave-vector space of a twin beam propagating in a nonlinear crystal in the regime with pump depletion. These waves start to develop at certain twin-beam intensity and move from the signal and idler beam centers towards their tails. They manifest themselves via the change of coherence volume monitored in the far field by the measurement of local modified $\bar{g}^{(2)}$ function, which acts as a sensitive and stable tool for investigating field intensity coherence.

I. INTRODUCTION

Coherence theory of light [1, 2] established in the 1950s completed the development of classical optics and gave the physicists a tool for investigating classical fields under the most general conditions. Importance of the classical coherence theory of light valid in general for intense fields, was also emphasized when its close similarity with the quantum coherence theory of light [3, 4], needed for weak nonclassical fields, was recognized using the theory of coherent states [5]. The general coherence theory allows us to successfully describe all possible optical fields, ranging from completely chaotic fields originating in spontaneous emission to maximally coherent fields that arise in stimulated emission. Wide possibilities for changing coherence properties of optical fields are provided by nonlinear (quantum) optics [3, 4, 6] in the framework of which mutual interactions of optical fields are analyzed. Nonlinearity then opens the door to the generation of nonclassical fields.

The generation of intense twin beams (TWBs), composed of a signal beam and an idler beam with shared photon pairs, emerging in the optical parametric process belongs to this area. Tight pairing of photons in TWBs even at the macroscopic level has been experimentally confirmed in Refs. [7–10] and used for ghost [11] and

quantum [12] imaging. The behavior of TWBs under various conditions was addressed in Refs. [13–23] in the usual regime with strong (un-depleted) pump. In this regime, TWB coherence increases as its intensity grows [13, 14] due to the prevailing stimulated emission. On the other hand, experimental investigations of Ref. [24] revealed that, in the regime with pump depletion, both spatial and spectral intensity coherence of a TWB do not necessarily have to increase with the increasing TWB intensity [24]. Numerical statistical simulations of the solution of the nonlinear Maxwell equations reported in [24] confirmed that pump-beam depletion leads to the fact that a TWB reaches its largest coherence at certain intensity depending on the configuration of the nonlinear interaction. The quantum theory of TWB generation [25–27], extended into the regime with pump depletion [28, 29], provided the physical explanation by decomposing the nonlinear interaction into many independent spatio-spectral modes [30] and analyzing their internal dynamics. Moreover, the theory in Ref. [28] pointed out at the existence of multiple coherence maxima in different intensity regimes of TWBs [31] and coherent components in otherwise chaotic TWBs [32]. Further, detailed analysis of local coherence in a TWB, provided by a model generalizing that of Ref. [28], revealed interesting behavior of local intensity coherence across the TWB profile during its evolution [33] whose observation is reported here. We note that the actual TWB intensities at which such a behavior is observed strongly depend on the value of the effective nonlinear coefficient, the interaction length as well as the pump-beam parameters [28].

^{*} radek.machulka@upol.cz

[†] jan.perina.jr@upol.cz

A pulse with spectral width around 1 nm and transverse profile of several hundreds of μ m containing $10^{14}-10^{15}$ photons allows to reach, in a BBO crystal several mm long, the regime with pump depletion and to generate in the process of parametric down-conversion a TWB containing $10^{12}-10^{14}$ photon pairs. On the other hand, pump pulses by several orders in magnitude weaker suffice to reach the regime of pump depletion when parametric down-conversion occurs in nonlinear photonic structures especially in nonlinear waveguides. A large number of independent spatio-spectral modes participating in parametric down-conversion represents the second necessary requirement for the observation of such a behavior.

A TWB, as it propagates along a nonlinear crystal, starts to develop from the vacuum state due to spontaneously emitted photon pairs that take their energy from a strong pump beam. At larger TWB intensities, stimulated emission of photon pairs prevails and this results in gradual improvement of TWB coherence, both in the spectral and (radial and azimuthal) wave-vector domains. We note that the TWB coherence is characterized, in general, by a coherence volume [4] spanned in the above three domains and determined in all the points of signal and idler beam profiles. Until the pump beam starts to be depleted, it holds that the greater the local signal (or idler) beam intensity the better the local coherence, as expected [13, 14]. However, when the pump beam is being depleted, dramatic changes in the evolution of TWB coherence occur: The area with the best coherence (i.e. with the largest coherence volume), originally localized in the signal (and idler) beam center starts to move towards the beam tails as the overall TWB intensity gradually increases. This forms waves in the coherence of the TWB that move in the signal and idler frequency and radial wave-vector beam profiles, as the TWB propagates along the crystal. These waves were recently theoretically predicted in Ref. [33]. We note that such waves in the coherence do not propagate along the azimuthal wave-vector axis in a radially symmetric TWB owing to constant signal- and idler-beam intensities along this axis. Here, by measuring the local modified $\bar{g}^{(2)}$ function, we experimentally investigate the behavior of waves in the TWB coherence.

II. THEORETICAL MODEL

In the model developed in Ref. [33, 34], the general nonlinear momentum operator \hat{G}_{int} of three mutually interacting beams propagating along the z axis,

$$\hat{G}_{\rm int}(z) = 2\epsilon_0 \int dx dy \int_{-\infty}^{\infty} dt \left[\chi^{(2)} : \hat{E}_{\rm p}^{(+)}(\mathbf{r}, t) \hat{E}_{\rm s}^{(-)}(\mathbf{r}, t) \hat{E}_{\rm i}^{(-)}(\mathbf{r}, t) + \text{H.c.} \right], \quad (1$$

is approximately replaced by the following momentum operator $\hat{G}_{\text{int}}^{\text{av}}$,

$$\hat{G}_{\text{int}}^{\text{av}}(z) = i\hbar \sum_{m=-\infty}^{\infty} \sum_{l,q=0}^{\infty} K_{mlq} \hat{a}_{p,mlq}(z) \hat{a}_{s,mlq}^{\dagger}(z) \hat{a}_{i,mlq}^{\dagger}(z) + \text{H.c.},$$
(2)

that effectively decomposes the three beams into many independent triplets of modes constituted by modes from each interacting beam. In Eq. (1), symbol $\hat{E}_{\rm p}^{(+)}$ [$\hat{E}_{\rm s}^{(-)}$, $\hat{E}_{\rm i}^{(-)}$] means the positive- [negative-] frequency part of the pump [signal, idler] electric-field operator amplitude, $\chi^{(2)}$ stands for the second-order susceptibility tensor, ϵ_0 is the permittivity of vacuum, H.c. replaces the Hermitian conjugated term, and $\mathbf{r}=(x,y,z)$. Annihilation [creation] operators $\hat{a}_{{\rm p},mlq}$ [$\hat{a}_{{\rm s},mlq}^{\dagger}$, $\hat{a}_{{\rm i},mlq}^{\dagger}$] in Eq. (2) belong to independent spatio-spectral modes in the corresponding beams indexed in azimuthal (m) and radial (l) wave-vector and frequency (q) variables, \hbar stands for the reduced Planck constant.

In the model, different effective nonlinear coupling constants K_{mlq} are assigned to individual mode triplets composed of the modes with different ability to build coherence. This gives us the key for the explanation of the coherence behavior: The initial exponential increase of intensities in the signal and idler modes of mode triplets leads to the gradual dominance of those modes experiencing the largest coupling constants, and thus having the ability to build the best coherence in the beam center. This is manifested by the decrease in the number of TWB modes [28, 35]. However, as already the classical solution of the three-mode interaction shows [33], the energy of pump modes in individual mode triplets is gradually completely depleted in the nonlinear interaction and back-flow of the energy towards the pump modes follows. This leads to the gradual loss of the dominance of the signal and idler modes with the largest coupling constants. This results in the enhancement of the role of the modes with smaller coupling constants and weaker ability to build coherence in the beam center. As a consequence, increase in the number of TWB modes occurs. On the other hand, due to the mutual phase synchronization, these modes are endowed with the ability to build highly coherent areas at the beam tails. It holds that, the smaller the coupling constants of the mode triplets prevailing in the TWB, the more distant the area with the largest coherence from the beam center. This is the way how the internal dynamics of mode triplets forms the waves in the coherence of evolving TWBs (for more details, see Ref. [33]).

A simplified qualitative physical explanation can be provided by considering the nonlinear interaction locally in the wave-vector and frequency domains. In the beam center, the largest local intensities occur and so the increase of coherence, followed by the gradual loss of coherence, develops the fastest. On the other hand, local intensities at beam tails are smaller, so the largest local

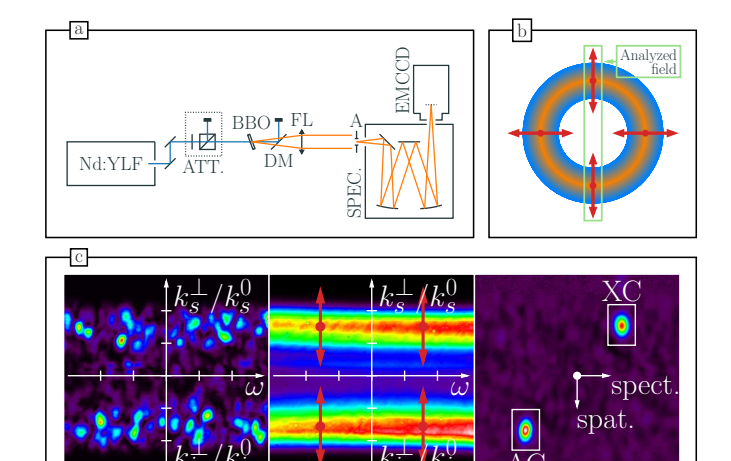
coherence is reached later. The more distant the area from the beam center, the lower the local intensities and so the later the largest local coherence is reached.

III. EXPERIMENTAL ARRANGEMENT

The waves in TWB coherence, that develop in the radial-wave vector domain during the TWB evolution along the nonlinear crystal towards the larger intensities, were observed in an experimentally feasible arrangement in which a nonlinear crystal of fixed length L is pumped by laser pulses with gradually increasing power P. The TWB coherence is analyzed beyond the crystal as it varies with the increasing power P. This approach relies on the fact that the three-mode interaction in the considered configuration evolves according to the parameter $L\sqrt{P}$ [6, 33], in which an increase of L can be equivalently substituted by an increase of \sqrt{P} . In detail, the experiment [24] was performed in the setup shown in Fig. 1(a) using a type-I BBO crystal of length L = 5 mm cut for frequency degenerate slightly noncollinear interaction. The crystal was pumped by the third-harmonic pulses (349 nm, 4.5-ps pulse duration) of a mode-locked regeneratively amplified Nd:YLF laser (High-Q-Laser) running at 500 Hz. Intensity spectrum of the pump pulses was 1.2 nm wide [full width at half maximum (FWHM)]. It was sufficiently broad to justify the application of the model discussed above. A halfwave plate followed by a polarizing-cube beam splitter was used to change the pump power P. The corresponding parts of the signal- and idler-beam emission cones [see Fig. 1(b)] were collected by a lens with 100-mm focal length and then collimated in the plane of the vertical slit of an imaging spectrometer (Andor Shamrock SR-300i, 1200 lines/mm grating). The angularly dispersed far-field radiation was recorded, shot by shot, by a synchronized EMCCD camera (iXon Ultra 897, Andor) operated at full-frame resolution (512x512 pixels, $16x16 \mu m^2$ pixel size). The presence of intensity correlations between the signal and idler beams was verified by observing symmetrically-positioned speckles around the degenerate wavelength and slightly non-collinear emission ($\theta_s = 1$ deg), as shown in Fig. 1(c). While the spectral correlations are observed in the horizontal directions, the spatial radial (wave-vector) correlations are visible in the vertical direction in Fig. 1(c).

IV. COHERENCE AND INTENSITY AUTO-CORRELATION FUNCTION

In principle, the adopted experimental arrangement allows us to directly follow the evolution in TWB coherence only in two degrees of freedom, radial wave-vectors and frequencies, via the measurement of the profiles of intensity auto-correlation functions. However, also the changes of the local coherence volume can be inferred



0.5

0.6

0.7

0.8

0.9

0.2

0.3

0.4

FIG. 1. (a) Experimental setup used for the determination of spatio-spectral intensity correlations in a TWB. Nd:YLF: pump laser; ATT.: varying pump-beam attenuation; BBO: nonlinear crystal; DM: dichroic mirror to deflect the pump beam; FL: Fourier lens with 100-mm focal length; A: aperture with vertical rectangular slit; SPEC.: imaging spectrometer; EMCCD: electron-multiplying CCD camera. (b) Ring formed by the signal-beam intensity in the far field for central frequency. (c) Output of the imaging spectrometer. From left to right: single-shot image of both beams showing the specklelike pattern with correlated grains, multiply-exposed image forming two horizontal strips (upper strip: signal beam, lower strip: idler beam) and scheme for the determination (observation) of intensity auto- (AC) and cross- (XC) correlations; color bar below quantifies the intensities in arbitrary units. In (c), the frequency axis ω extends from 677.3 nm to 718.7 nm, the signal (k_s^{\perp}) and idler (k_i^{\perp}) radial wave-vector axes cover the range from 0 mrad to 40 mrad. In (b) and (c), red arrows indicate the propagation of waves in TWB coherence at increasing TWB intensity. They start to develop above certain threshold pump-power $P_{\rm th}$.

from the measurement of the normalized intensity autocorrelation function $\bar{g}^{(2)}$ [see Eq. (3) below] performed in a detection volume with a suitably chosen finite size [determined by the area of (grouped) pixel(s) of the CCD chip and width of the slit in the beams' transverse plane that defines the analyzed fields. As the simple 1D model presented below shows, the extension of the 3D detector in at least one dimension has to be comparable to the corresponding coherence length to allow for the observation of changes in this coherence length via the observation of the $\bar{g}^{(2)}$ function. Since the direct observation of coherence changes in radial wave-vector and frequency domains via the corresponding intensity auto-correlation functions $A_{s,k}$ and $A_{s,\omega}$, respectively, requires an experimental geometry with 'tiny pixels' on the camera to reach sufficient precision, we used a suitably wide slit in the vertical plane of the input to the imaging spectrometer to allow for changes in the $\bar{g}^{(2)}$ function.

The normalized modified $\bar{g}^{(2)}$ function measured in a

given detection volume V is defined as

$$\bar{g}^{(2)} = \frac{\langle (\Delta W)^2 \rangle}{\langle W \rangle^2} = \frac{\langle W^2 \rangle}{\langle W \rangle^2} - 1 = g^{(2)} - 1 \tag{3}$$

in terms of the moments of the overall detection intensity $W = \int_V d\mathbf{r} I(\mathbf{r})$ and its fluctuation $\Delta W = W - \langle W \rangle$ or using the usual $g^{(2)}$ function. We note that, according to the definition in Eq. (3), $\bar{g}^{(2)}=1$ for a singlemode thermal beam. A general relationship between the $\bar{q}^{(2)}$ function and local beam coherence can be understood by considering an M-mode thermal optical field with equally populated modes defined in the detection volume. In this case, we have $\bar{g}^{(2)} = 1/M$ [4]. Thus the larger the function $\bar{q}^{(2)}$ the smaller the number M of local modes and consequently the better the local coherence (the greater the coherence volume). To quantify the relationship between the modified $\bar{g}^{(2)}$ function and coherence volume, we first consider a 1D model in which a pixel of extension 2d is illuminated by a spatially stationary beam with (point) intensity $I(x) \equiv I_0$ and intensity spatial correlation function $\langle \Delta I(x)\Delta I(x')\rangle \equiv \mathcal{I}(x-x')$, with $\Delta I(x) = I(x) - I_0$. Assuming a Gaussian intensity auto-correlation function $\mathcal{I}(x) = \exp[-x^2/(\Delta A)^2]$ with ΔA giving the coherence length, the corresponding modified $\bar{g}_{1D}^{(2)}$ function attains the form:

$$\bar{g}_{1D}^{(2)} = \frac{\int_{-d}^{d} dx \int_{-d}^{d} dx' \langle \Delta I(x) \Delta I(x') \rangle}{\left[\int_{-d}^{d} dx \langle I(x) \rangle \right]^{2}}$$
$$= \frac{\sqrt{\pi}}{2} \frac{\Delta A}{d} \operatorname{erf} \left(\frac{d}{\Delta A} \right); \tag{4}$$

erf $(x)=(2/\sqrt{\pi})\int_0^x dt \exp(-t^2)$. According to Eq. (4), we have $\bar{g}_{\rm 1D}^{(2)} \to 1$ for $\Delta A \gg d$, i.e. a fully spatially coherent field is composed of just one mode. On the other hand, $\bar{g}_{\rm 1D}^{(2)} \to 0$ in the opposite case $\Delta A \ll d$ of a weakly spatially coherent field composed of many modes. The graph of $\bar{g}_{\rm 1D}^{(2)}$ function of Eq. (4), plotted in Fig. 2(a), points out a strong sensitivity of the $\bar{g}_{\rm 1D}^{(2)}$ function on the normalized coherence length $\Delta a \equiv \Delta A/d$ for $\Delta a_x \in \langle 0.2, 3 \rangle$. Assuming for simplicity the factorized intensity correlation functions in 3D model, the above 1D model is appropriate in all the three dimensions: radial and azimuthal wave-vectors and spectral. For comparison, the behavior of $\bar{g}_{\rm 1D}^{(2)}$ function derived from the measurement in frequency and radial wave-vector directions by fixing the coherence length (signal-beam center, at threshold power $P_{\rm th}$) and varying the detector width (grouping of pixels) is shown in Fig. 2(b).

V. OBSERVATION OF WAVES IN TWB COHERENCE

To document close similarity in the behavior of the modified $\bar{g}^{(2)}$ function and widths $\Delta A_{s,\varphi}$, $\Delta A_{s,\omega}$ and

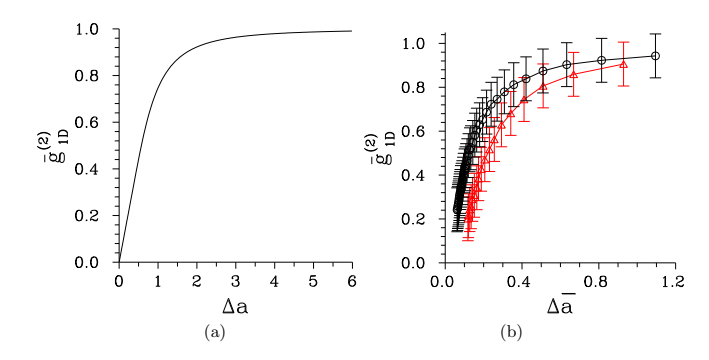


FIG. 2. Functions (a) $\bar{g}_{1\mathrm{D}}^{(2)}(\Delta a)$ from Eq. (4) of the Gaussian model and (b) $\bar{g}_{1\mathrm{D}}^{(2)}(\Delta \tilde{a})$ derived from the experimental data by grouping the pixels in the spectral (red Δ) and radial wave-vector (black \circ) directions as they depend on normalized coherence lengths $\Delta a = \Delta A/d$ and $\Delta \tilde{a} = \sqrt{\ln(2)}\Delta a$. In (b), solid curves connect the experimental points.

 $\Delta A_{\mathrm{s},k}$ of intensity auto-correlation functions in the azimuthal wave-vector (φ) , frequency (ω) and radial wavevector (k) directions, respectively, we draw their dependence on pump power P in the signal-beam center in Fig. 3. All four quantities increase at increasing pump power P below the threshold power $P_{\rm th} \approx 70 \text{ mW}$ $(2.45 \times 10^{14} \text{ photons per single pump pulse})$ as a consequence of the gradual increase of TWB coherence in all three directions. Then, for higher pump powers, coherence is partially lost due to the gradual increase of the number of effectively-populated TWB modes, as discussed above. The theoretical curves displayed in Fig. 3 originate in the model of a spatially and spectrally multimode TWB of Ref. [33], in which we assume a Gaussian pump pulsed beam at wavelength 349 nm, with repetition rate 500 Hz, being 230 µm wide (intensity FWHM, at the input crystal plane) and having temporal spectrum 1.2 nm wide (intensity FWHM) together with a BBO crystal 4 mm long. The crystal phase matching was such that the signal beam leaved the crystal at $\theta_s^0 = 1.0$ deg. The model predicts 2.29×10^{12} photon pairs per single pump pulse at P = 70 mW.

The experimental modified $\bar{g}^{(2)}$ function and the corresponding local number $M_g \equiv 1/\bar{g}^{(2)}$ of modes per single pixel measured in the signal-beam strip at the central frequency ω_s^0 are drawn in Figs. 4(a) and (c) as a function of the varying normalized radial wave vector $k_{\rm s}^{\perp}/k_{\rm s}^0$ and pump power P. Their theoretical counterparts are also shown in Figs. 4(b) and (d), respectively. Splitting of the maximum of the $\bar{g}^{(2)}$ function in the radial wavevector direction (k_s^{\perp}/k_s^0) for the pump powers higher than $P_{\rm th} \approx 70$ mW is evident in the graph in Fig. 4(a). The maximum splits at $P_{\rm th}$ into two local maxima that move towards the low and high radial wave-vectors k_s^{\perp} , i.e. towards the signal-beam tails. This movement at increasing pump power P, and hence at increasing overall TWB intensity, exhibits the propagation of waves in TWB coherence during the TWB evolution. The positions of the (local) maxima in the signal-beam radial wave-vector di-

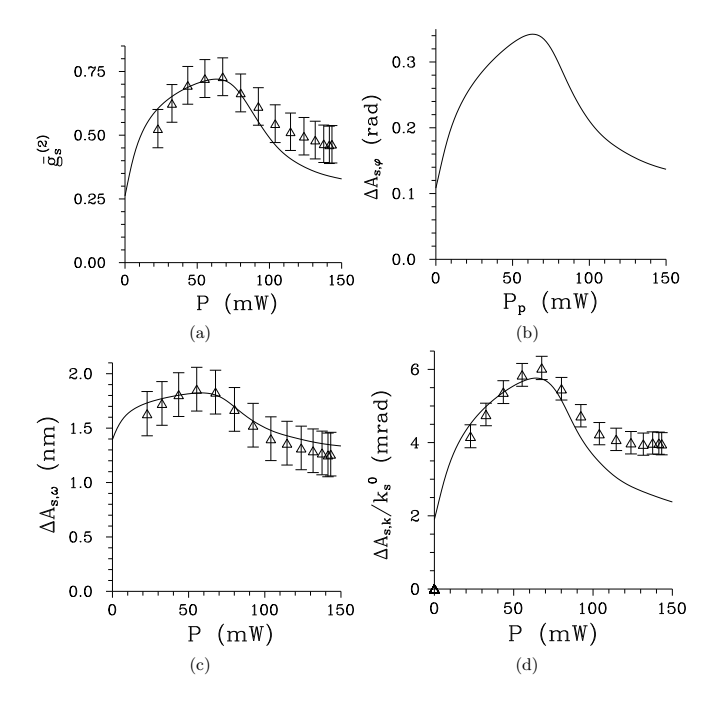


FIG. 3. (a) Function $\bar{g}^{(2)}$ measured at individual pixels and widths (b) $\Delta A_{s,\varphi}$, (c) $\Delta A_{s,\omega}$ and (d) $\Delta A_{s,k}$ of, in turn, azimuthal wave-vector, spectral and radial wave-vector intensity auto-correlation functions (FWHM) for the signal beam at central frequency ω_s^0 and central radial wave vector k_s^0 as they depend on pump power P. Experimental data are plotted as isolated symbols with error bars, solid curves originate in the theoretical model [33].

rection as they evolve at increasing pump power P are drawn in Fig. 5. Similarly, typical profiles of $\bar{q}^{(2)}$ function in the signal-beam radial wave-vector direction are shown in Fig. 6 for fixed pump powers P. The modulation of $\bar{g}^{(2)}$ function along the signal radial wave-vector direction is dominantly caused by the variation of coherence length with the pump power in the azimuthal wavevector direction. This is so since the pixel widths in the frequency (0.083 nm) and radial wave-vector (0.16 mrad) directions are by one order in magnitude smaller than the corresponding coherence lengths. To verify the method of monitoring the TWB coherence via the measurement of $\bar{q}^{(2)}$ function, we summed the intensities from 4 and 8 neighboring pixels for both directions on the EMCCD and observed a decrease in the values of $\bar{q}^{(2)}$ function, as documented in Fig. 7. It holds that the wider the detection area on EMCCD, the smaller the $\bar{q}^{(2)}$ function, the larger the number of local modes and so the worse the local coherence in the detection area.

In the experiment, the waves in TWB coherence along the signal radial wave-vector profile were also observed by directly monitoring the widths $\Delta A_{s,\omega}$ and $\Delta A_{s,k}$ of frequency and radial wave-vector intensity autocorrelation functions. However, as evidenced in Figs. 4(e) and (f), these widths are determined from the experimental data with considerably larger fluctuations than the $\bar{g}^{(2)}$ function in Fig. 4(a). Good 'stability' of the measurement

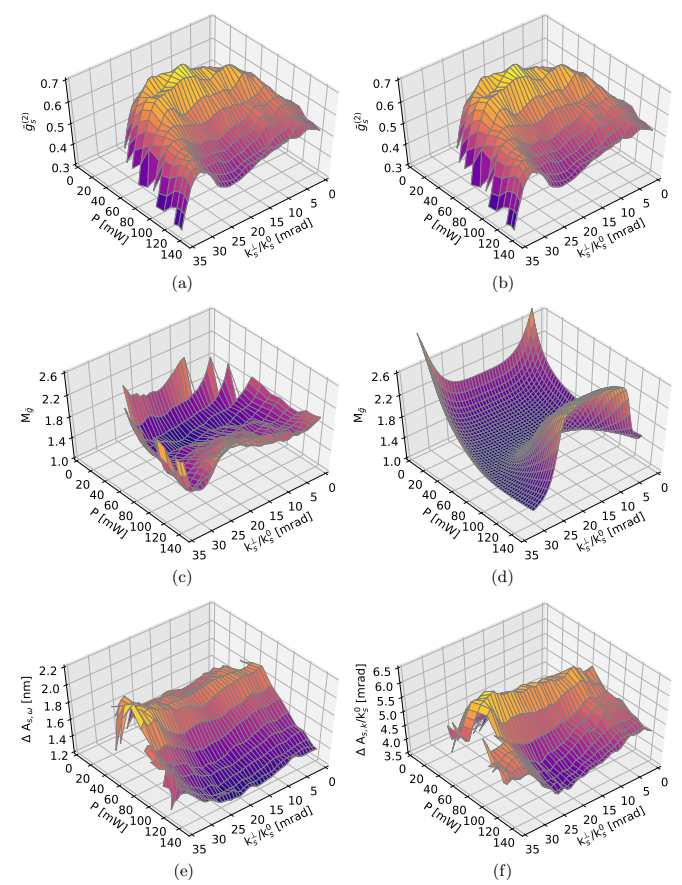


FIG. 4. (a) Experimental and (b) theoretical $\bar{g}^{(2)}$ function for individual pixels, (c) experimental and (d) theoretical number $M_g=1/\bar{g}^{(2)}$ of local modes and experimental widths (e) $\Delta A_{\mathrm{s},\omega}$ and (f) $\Delta A_{\mathrm{s},k}$ of frequency and radial wave-vector, respectively, intensity autocorrelation functions [FWHM] as they depend on normalized radial wave vector $k_\mathrm{s}^\perp/k_\mathrm{s}^0$ and pump power P for the central signal-beam frequency ω_s^0 . Relative errors are better than 5% in (f), 11% in (e) and 12% in (a,c).

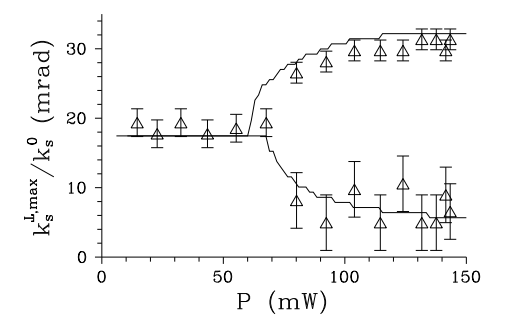


FIG. 5. Positions of maxima of $\bar{g}^{(2)}$ function drawn in Figs. 4(a) and (b) in signal-beam radial wave vector $k_{\rm s}^{\perp}$ as they depend on pump power P. Experimental (theoretical) data are plotted as isolated symbols (by solid curves).

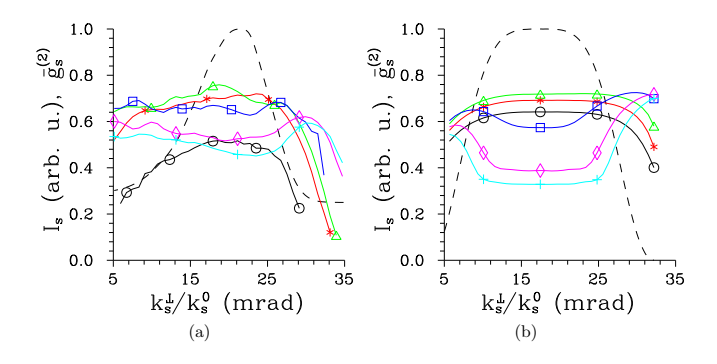


FIG. 6. (a) Experimental and (b) theoretical profiles of the signal-beam $\bar{g}^{(2)}$ function drawn in Fig. 4 [relative errors better than 12%] along normalized radial wave vector k_s^{\perp}/k_s^0 for powers P equal to 23 mW [30 mW] (solid curves with black \circ), 43 mW [45 mW] (red *), 55 mW [60 mW] (green \triangle), 80 mW [90 mW] (blue \square), 115 mW [120 mW] (magenta \diamond) and 142 mW (150 mW) (cyan +) drawn in (a) [(b)]. Signal-beam intensity profile $I_{s,k}$ [relative error 1%] is drawn by dashed curves.

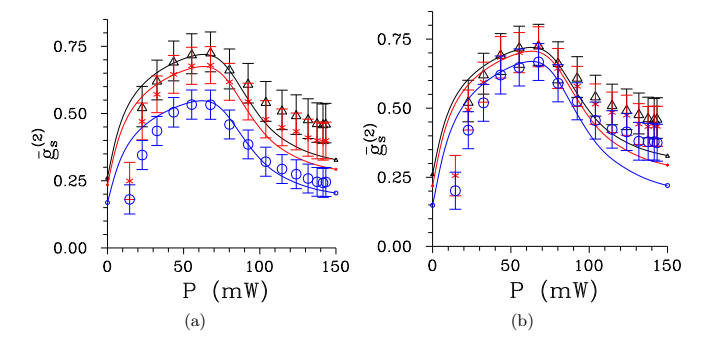


FIG. 7. Functions $\bar{g}^{(2)}$ obtained by grouping 1 (black \triangle), 4 (red *), and 8 (blue \circ) pixels in (a) frequency and (b) radial wave-vector directions for the signal beam at central frequency $\omega_{\rm s}^0$ and central radial wave vector $k_{\rm s}^{\perp 0}$ as they depend on pump power P. Experimental data are plotted as isolated symbols with error bars, solid curves originate in the theoretical model.

of $\bar{g}^{(2)}$ function comes from its natural 3D character (intensity in its definition is integrated over the detection volume) that remains also in our configuration with the dominant influence from only the azimuthal wave-vector direction. This, together with strong sensitivity to coherence changes (see Fig. 2) makes the measurement of $\bar{g}^{(2)}$ function superior for the observation of coherence variations.

Before we conclude, we note that the waves in TWB coherence propagate also along the spectral (frequency) profiles of the signal and idler beams, similarly to those

observed along the radial wave-vector profiles. Nevertheless, the signal- and idler-beam spectra generated from the BBO crystal are relatively wide and so only a fraction of them is experimentally analyzed [see Fig. 1(c)]. Such configuration is not suitable for the observation of coherence waves. We also note that the agreement between the experimental and theoretical behaviors of the analyzed $\bar{g}^{(2)}$ functions is in some cases only qualitative [Figs. 4(a,b), 6(a,b)]. The reason is that the theoretical model of Ref. [33] does not include birefringence of the BBO crystal (walk-off effects modelled by the effective shortening of the interaction length) and considers pump beams with Gaussian spatial and temporal spectra (contrary to multi-mode high-intense experimental pump beams).

VI. CONCLUSIONS

The waves in twin-beam coherence, developing as the twin beam evolves (increases its energy) in the nonlinear process, were indirectly observed in the signal-beam profile in the radial wave-vector direction using the configuration with a crystal of fixed length illuminated by a pump beam with varying power. In the far field of the signal and idler beams, i.e. in their transverse wave-vector spaces, these waves attain a ring-shaped form. They propagate from the beams' centers towards their tails in the radial wave-vector direction as the twin-beam intensity increases during its evolution. Similar waves occur also in the spaces spanned by azimuthal wave vector and frequency. These waves in 2D spaces, in fact, represent projections of the waves in twin-beam coherence formed in the signal- and idler-beam 3D wave-vector spaces. The waves in twin-beam coherence were indirectly monitored via the suggested measurement of changes of the local modified $\bar{g}^{(2)}$ function registered in the volume of individual pixels at EMCCD camera. Higher sensitivity of the modified $\bar{g}^{(2)}$ function to the changes of coherence compared to direct measurement of widths of intensity auto-correlation functions in three orthogonal directions was successfully utilized.

ACKNOWLEDGMENTS

The authors thank the bilateral Czech-Italian project CNR-16-05 between CAS and CNR and projects No. 18-08874S by GA ČR (R.M. and O.H.) and No. 18-22102S by GA ČR (J.P.). Support from the project No. CZ.1.05/2.1.00/19.0377 of MŠMT ČR is also acknowledged.

M. Born and E. Wolf, Principles of Optics, 6th ed. (Pergamon Press, Oxford, 1980).

- [3] L. Mandel and E. Wolf, Optical Coherence and Quantum Optics (Cambridge Univ. Press, Cambridge, 1995).
- [4] J. Peřina, Quantum Statistics of Linear and Nonlinear Optical Phenomena (Kluwer, Dordrecht, 1991).
- [5] R. J. Glauber, "Coherent and incoherent states of the radiation field," Phys. Rev. 131, 2766—2788 (1963).
- [6] R. W. Boyd, Nonlinear Optics, 3rd edition (Elsevier, Amsterdam, 2008).
- [7] O. Jedrkiewicz, Y. K. Jiang, E. Brambilla, A. Gatti, M. Bache, L. A. Lugiato, and P. Di Trapani, "Detection of sub-shot-noise spatial correlation in high-gain parametric down-conversion," Phys. Rev. Lett. 93, 243601 (2004).
- [8] M. Bondani, A. Allevi, G. Zambra, M. G. A. Paris, and A. Andreoni, "Sub-shot-noise photon-number correlation in a mesoscopic twin beam of light," Phys. Rev. A 76, 013833 (2007).
- [9] J.-L. Blanchet, F. Devaux, L. Furfaro, and E. Lantz, "Measurement of sub-shot-noise correlations of spatial fluctuations in the photon-counting regime," Phys. Rev. Lett. 101, 233604 (2008).
- [10] G. Brida, L. Caspani, A. Gatti, M. Genovese, A. Meda, and I. R. Berchera, "Measurement of sub-shot-noise spatial correlations without backround subtraction," Phys. Rev. Lett. 102, 213602 (2009).
- [11] A. Gatti, E. Brambilla, and L. Lugiato, "Quantum imaging," in *Progress in Optics*, Vol. 51, edited by E. Wolf (Elsevier, Amsterdam, 2008) pp. 251—348.
- [12] G. Brida, M. Genovese, and I. R. Berchera, "Experimental realization of sub-shot-noise quantum imaging," Nature Phot. 4, 227—230 (2010).
- [13] A. Gatti, R. Zambrini, M. San Miguel, and L. A. Lugiato, "Multiphoton multimode polarization entanglement in parametric down-conversion," Phys. Rev. A 68, 053807 (2003).
- [14] E. Brambilla, A. Gatti, M. Bache, and L. A. Lugiato, "Simultaneous near-field and far-field spatial quantum correlations in the high-gain regime of parametric downconversion," Phys. Rev. A 69, 023802 (2004).
- [15] E. Brambilla, L. Caspani, L. A. Lugiato, and A. Gatti, "Spatiotemporal structure of biphoton entanglement in type-II parametric down-conversion," Phys. Rev. A 82, 013835 (2010).
- [16] L. Caspani, E. Brambilla, and A. Gatti, "Tailoring the spatiotemporal structure of biphoton entanglement in type-I parametric down-conversion," Phys. Rev. A 81, 033808 (2010).
- [17] A. Christ, K. Laiho, A. Eckstein, K. N. Cassemiro, and C. Silberhorn, "Probing multimode squeezing with correlation functions," New J. Phys. 13, 033027 (2011).
- [18] M. Stobińska, F. Töppel, P. Sekatski, and M. V. Chekhova, "Entanglement witnesses and measures for bright squeezed vacuum," Phys. Rev. A 86, 022323 (2012).
- [19] A. M. Pérez, T. S. Iskhakov, P. Sharapova, S. Lemieux, O. V. Tikhonova, M. V. Chekhova, and G. Leuchs,

- "Bright squeezed-vacuum source with 1.1 spatial mode," Opt. Lett. **39**, 2403—2406 (2014).
- [20] M. V. Chekhova, G. Leuchs, and M. Zukowski, "Bright squeezed vacuum: Entanglement of macroscopic light beams," Opt. Comm. 337, 27—43 (2015).
- [21] P. Sharapova, A. M. Pérez, O. V. Tikhonova, and M. V. Chekhova, "Schmidt modes in the angular spectrum of bright squeezed vacuum," Phys. Rev. A 91, 043816 (2015).
- [22] A. Cavanna, F. Just, P. R. Sharapova, M. Taheri, G. Leuchs, and M. V. Chekhova, "Tunable optical parametric generator based on the pump spatial walk-off," Opt. Lett. 41, 646—649 (2016).
- [23] M. V. Chekhova, S. Germanskiy, D. B. Horoshko, G. K. Kitaeva, M. I. Kolobov, G. Leuchs, C. R. Phillips, and P. A. Prudkovskii, "Broadband bright twin beams and their upconversion," Opt. Lett. 43, 375—378 (2018).
- [24] A. Allevi, O. Jedrkiewicz, E. Brambilla, A. Gatti, J. Peřina Jr., O. Haderka, and M. Bondani, "Coherence properties of high-gain twin beams," Phys. Rev. A 90, 063812 (2014).
- [25] C. K. Law, I. A. Walmsley, and J. H. Eberly, "Continuous frequency entanglement: Effective finite Hilbert space and entropy control," Phys. Rev. Lett. 84, 5304—5307 (2000).
- [26] C. K. Law and J. H. Eberly, "Analysis and interpretation of high transverse entanglement in optical parametric down-conversion," Phys. Rev. Lett. 92, 127903 (2004).
- [27] M. V. Fedorov and M. I. Miklin, "Schmidt modes and entanglement," Contemporary Phys. 55, 94—109 (2014).
- [28] J. Peřina Jr., "Spatial, spectral and temporal coherence of ultra-intense twin beams," Phys. Rev. A 93, 013852 (2016).
- [29] J. Peřina Jr., "Intense spectrally broad-band twin beams from poled nonlinear crystals," Sci. Rep. 8, 015350 (2018).
- [30] J. Peřina Jr., "Coherence and mode decomposition of weak twin beams," Phys. Scr. 90, 074058 (2015).
- [31] J. Peřina Jr., O. Haderka, A. Allevi, and M. Bondani, "Internal dynamics of intense twin beams and their coherence," Sci. Rep. 6, 22320 (2016).
- [32] J. Peřina Jr., "Coherent light in intense spatiospectral twin beams," Phys. Rev. A 93, 063857 (2016).
- [33] J. Peřina Jr., "Waves in spatio-spectral and -temporal coherence of evolving ultra-intense twin beams," Sci. Rep. 9, 4256 (2019).
- [34] J. Peřina Jr., "Coherence and dimensionality of intense spatio-spectral twin beams," Phys. Rev. A 92, 013833 (2015).
- [35] G. Triginer, M. D. Vidrighin, N. Quesada, A. Eckstein, M. Moore, W. S. Kolthammer, J. E. Sipe, and I. A. Walmsley, "Understanding high gain twin beam sources using cascaded stimulated emission," arXiv, 1911.05708 (2019).